Tunable nonlocal valley-entangled Cooper pair splitter realized in bilayer-graphene van der Waals spin valves

Xiuqiang Wu [1,*] Hao Meng [2] Fanjie Kong,[1] Haiyang Zhang [1] Yujie Bai,[1] and Ning Xu[1,†]
[1]*Department of Physics, Yancheng Institute of Technology, Yancheng 224051, China*
[2]*School of Physics and Telecommunication Engineering, Shaanxi University of Technology, Hanzhong 723001, China*

(Received 7 August 2019; revised manuscript received 18 February 2020; accepted 20 February 2020; published 9 March 2020)

We investigate the Cooper pair splitting based on crossed Andreev reflection in a two-dimensional narrow superconductor coupled to two leads, where the two leads are van der Waals (vdW) spin valves formed by inserting bilayer graphene (BLG) between two antiparallel insulating ferromagnetic layers. In this BLG-based *n*-type vdW spin valve/superconductor/*p*-type vdW spin valve junction with edge-contact geometry, when controlling the Fermi energy and the interlayer electric field in BLG independently by top- and bottom-gate voltages in the vdW spin valve region, we first demonstrate that the two electrons of perfect Cooper pair splitting can remain nonlocal valley entanglement. This effect can be explained as follows: When both the two antiparallel insulating ferromagnetic layers and the interlayer electric field are taken into account, BLG exhibits a spin-splitting but valley-degenerate band gap near the Dirac point. Thus, our setups allow the Cooper pair in the BCS scenario to serve as a natural source of valley entanglement. We further predict large oscillations of cross conductance as a function of the doping of the superconductor, the junction length, and the bias voltage. Our results may provide a tool for realizing fast nonlocal switching of the valley-entanglement state.

DOI: 10.1103/PhysRevB.101.125406

I. INTRODUCTION

Quantum entanglement between two particles is a fundamental feature of quantum mechanics in which the state of one particle is determined by a measurement performed on the other [1]. This feature has been identified as a useful property for applications in both computation and communication [2]. For example, entanglement between photons is well developed and already offers applications [3–5]. In the solid state, entangled electrons can be exploited as a source of Einstein-Podolsky-Rosen pairs, which is a necessary ingredient for the teleportation of qubit states across a chip [6–8]. Proposals for nonlocally entangled electron pairs have been put forward [9–13]. One attractive proposal is splitting the Cooper pairs in a BCS superconductor via crossed Andreev reflection (CAR) into spatially separated leads. This idea has so far motivated numerous theoretical and experimental attempts to split Cooper pairs in various geometries and materials, such as ferromagnetic junctions [14–18], *p*-*n* junctions [19–21], topological systems [22–24], quantum dots [25–27], carbon nanotubes [28–30], bilayer graphene (BLG) [31], and quantum hall systems [32]. In these endeavors, the Cooper pair splitter is either nonlocal spin-entangled electrons [19–21,25,26,31,33] or not spin entangled due to spin helicity or spin polarization of the leads [14–18,22–24,27,33–37]. In principle, a Cooper pair in the BCS scenario can also serve as a source of spatially separated entangled electrons with momentum. An earlier work proposed a spin-independent scheme to generate momentum-entangled electron pairs via CAR in a mesoscopic normal-superconductor system [38]. However, this method has the drawback that full cancelation of local AR is only at precise tuning the splitter from open to close.

Due to the existence of two valleys related by time-reversal symmetry in two-dimensional (2D) hexagonal crystals such as graphene, silicene, MoS_2 and other group-VI dichalcogenides, the two electrons at the two inequivalent valleys with opposite spins can form Cooper pairs in the BCS ground state, which are natural candidates to study the process of AR at the normal-superconducting interface in which the incident electron and the reflected hole come from the different valleys [16,39–45]. Since the Cooper pairs consist of two electrons that are both spin and momentum entangled, they can, in principle, serve as a source of spatially separated valley-entangled electrons if such Cooper pairs can be extracted coherently. Although there has been great interest in the properties of the splitting of Cooper pairs in 2D hexagonal crystals, the common mechanism for such a Cooper pair beam splitter relies on the spin singlet character of Cooper pairs; the study of devices combining valley degrees of freedom and quantum entanglement via CAR is still in its infancy. Meanwhile, it is important to point out that the large momentum separation between different valleys causes the suppression of intervalley scattering so that the electron subsystems near K and K' points are effectively independent. Thus, slow valley relaxation and dephasing processes, compared to electron spin, can be accessed [46,47]. We also remark that the search for novel systems realizing nonlocal valley-entangled electron pairs can

*xianqiangzhe@126.com
†nxu@ycit.cn

provide a unique playground to test the interplay between transport and electron correlations.

Motivated by these interesting features, in the present work we propose, guided by the finding that AB-stacked BLG can open a band gap at the two inequivalent corners of the Brillouin zone by adjusting the gate voltages [48] or the van der Waals (vdW) spin valve [49,50], a strategy for realizing a nonlocal valley-entangled Cooper pair splitter in AB-stacked BLG vdW spin valves. Making use of the two antiparallel insulating ferromagnetic (AIF) layers and the interlayer electric field, the band structure of BLG has a spin-dependent but valley-degenerated band gap near the Dirac points. When controlling the Fermi energy and the interlayer electric field independently by tuning the top and bottom gates in the vdW spin valve region, we demonstrate that the local AR and the elastic cotunneling (EC) are completely blocked, while local normal reflection (NR) and perfect CAR are the only permissible process. As a consequence of this perfect CAR, two electrons of a Cooper pair in a conventional BCS superconductor (SC) can be split towards opposite leads and remain valley entangled. Moreover, we find that the corresponding cross conductance exhibits largely oscillatory behavior when the doping of the SC, the junction length, and the bias voltage is varied. This large oscillation may find promising applications in a valley-entangled switch.

II. MODEL AND FORMALISM

The starting point for BLG with AB stacking is the effective four-band Hamiltonian near the centers of the valleys in the basis A_1, B_1, A_2, B_2, with A (B) and 1 (2) labeling the sublattice and layer numbers [51–54],

$$H = \begin{pmatrix} \varepsilon_{A_1} & \hbar v_F \pi_- & 0 & 0 \\ \hbar v_F \pi_+ & \varepsilon_{B_1} & \gamma & 0 \\ 0 & \gamma & \varepsilon_{A_2} & \hbar v_F \pi_- \\ 0 & 0 & \hbar v_F \pi_+ & \varepsilon_{B_2} \end{pmatrix},$$
$$\pi_\pm = \eta k_x \pm i k_y, \tag{1}$$

where $v_F = \sqrt{3} a \gamma_0 / 2\hbar \approx 10^6\ \mathrm{m\,s^{-1}}$ is the effective Fermi velocity, $\gamma = 0.38$ eV is the interlayer nearest-neighbor hopping, ϵ_{m_i} $(m = A, B; i = 1, 2)$ is the on-site energy, and (k_x, k_y) are the 2D kinematic momenta for states at the two inequivalent corners, K and K', of the Brillouin zone with $\eta = \pm$ labeling the two valleys. The factor $\hbar v_F$ will be set to 1 in the following, unless stated otherwise.

To enable unexplored device opportunities, we study the effects of proximity in vdW heterostructures that can engineer electronic structures of a 2D material through its adjacent regions, which do not occur naturally within a single 2D material. In the presence of a double-gate voltage and two AIF layers (see Fig. 1), the on-site energy due to the proximity effect is modeled as [49,50,55]

$$\varepsilon_{A_1} = \varepsilon_{B_1} = \lambda_s^+ - U,$$
$$\varepsilon_{A_2} = \varepsilon_{B_2} = \lambda_{-s}^- - U, \tag{2}$$

where $\lambda_s^\pm = \pm\lambda_E + sM$ is a Dirac mass term. Here, λ_E is the potential difference which can open a band gap at the charge neutral point. U is the electrostatic potential between on-site energies in the two layers. sM is a spin-dependent band gap with $s = \uparrow(+), \downarrow(-)$. Note that the sign of s can be reversed by changing the AIF configuration [49].

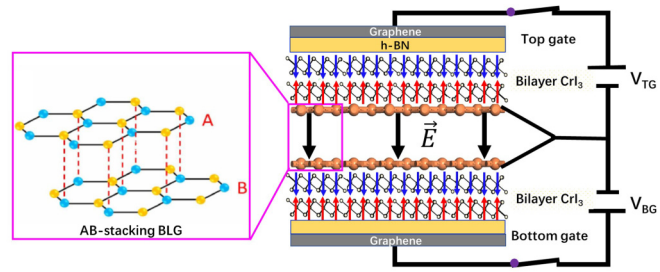

FIG. 1. Schematic of a CrI_3-encapsulated dual-gated BLG device geometry. The total doping density n and the vertical electric field $\vec{E}$ in graphene bilayers are governed by the top- and bottom-gate voltages V_{TG} and V_{BG} in this dual-gate field-effect device. This device simultaneously enables the electrical control of magnetism in bilayer CrI_3.

To electrically gate BLG, we use the dual-gated structure which has BLG fully encapsulated by the magnetic insulator bilayer CrI_3 [56] (see Fig. 1). Hexagonal boron nitride (h-BN) flakes serve as a flat and clean dielectric environment between the BLG and the top and bottom gates. We also use graphene as top- and bottom-gate electrodes, which enable a reversible electrical switching of magnetic order in the CrI_3 AIF layer near the interlayer spin-flip transition [57,58]. On the other hand, voltages applied on top and bottom gates (V_{TG} and V_{BG}) simultaneously enable us to independently control the interlayer potential difference λ_E and the electrostatic potential U in the BLG [54,59–62].

Within this model, we consider the energy spectrum of the bilayer graphene system described by Eqs. (1) and (2). The energy eigenvalues read

$$E_{\pm,s}^{\alpha,\varepsilon} = \varepsilon \sqrt{k^2 + (\lambda_s^\pm)^2 + \frac{\gamma^2}{2} + (-)^\alpha \sqrt{\left(\frac{\gamma^2}{2}\right)^2 + k^2[4(\lambda_s^\pm)^2 + \gamma^2]}}, \tag{3}$$

with $\alpha = 1, 2$. $k = \sqrt{k_x^2 + k_y^2}$ represents a wave vector measured from the two inequivalent valley points K and K'. The index $\varepsilon = \pm$ specifies the conduction and valance bands. Since the higher-energy band $E_{\pm,s}^{2,\varepsilon}$ is not convenient for the analysis of transport properties of carriers in the low-energy band of a bilayer [51], we neglect the contribution of carriers in the higher-energy band $E_{\pm,s}^{2,\varepsilon}$, as shown in Fig. 2.

From the low-energy spectrum for the BLG in the presence or absence of the spin-dependent potential M and potential difference λ_E, calculated from Eq. (3), we observe the following: (i) When M or λ_E is separately turned on, a gap appears while spin and valley states are degenerate in the conduction and valence bands, as shown in Figs. 2(a) and 2(e) and 2(b) and 2(f). The gap between conduction and valence band edges is given by $2\lambda_s$ for $k = 0$. (ii) For $\lambda_E \neq 0$ and $M \neq 0$, the combination of potential difference λ_E and spin-dependent potential M opens a gap and splits

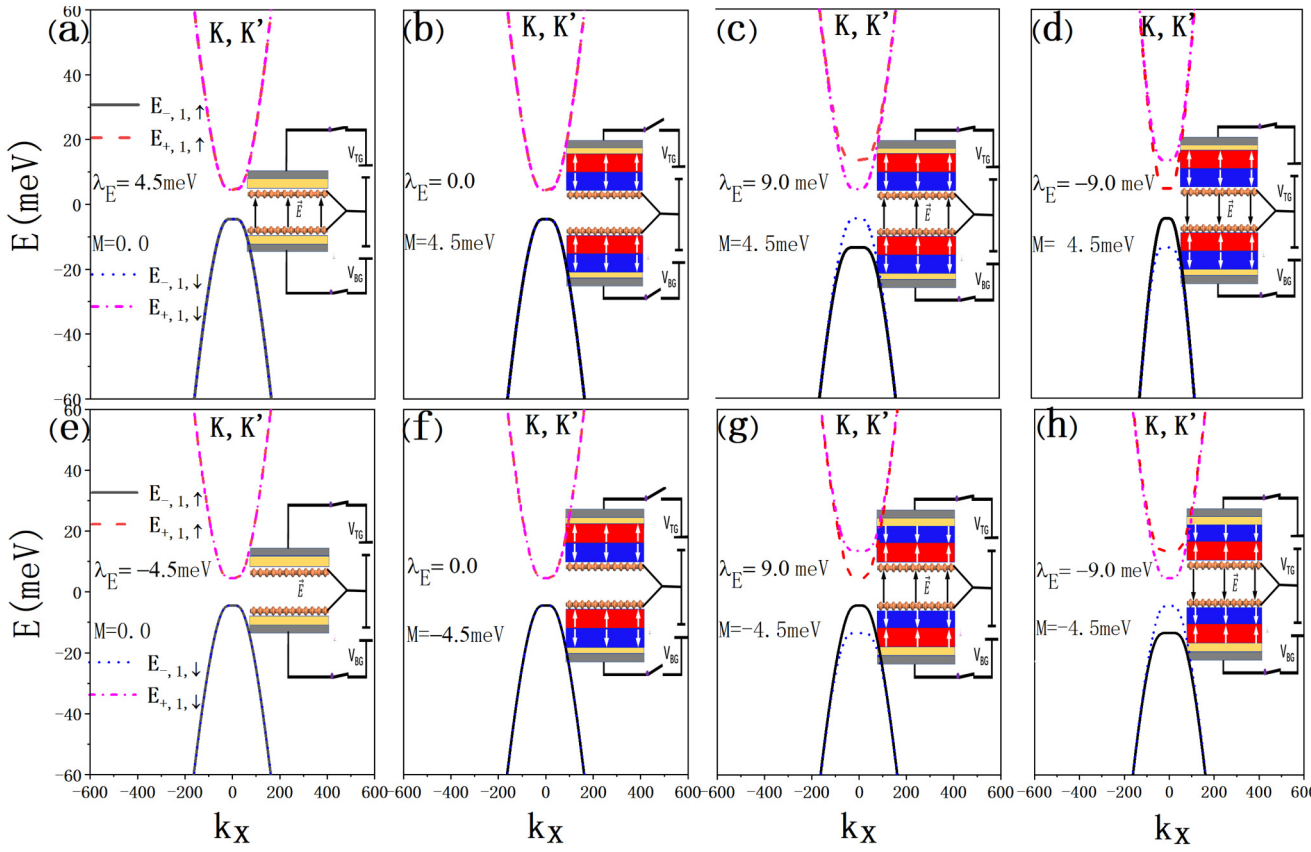

FIG. 2. Effects of spin-dependent potential M and potential difference λ_E on the low-energy bands $E^{1,\varepsilon}_{\pm,s}$ of bilayer graphene plotted along the k_x axis near the corners K, K'. (a) and (e) $M = 4.5$ meV, $\lambda_E = 0.0$ and $M = -4.5$ meV, $\lambda_E = 0.0$; (b) and (f) $M = 0.0$, $\lambda_E = 4.5$ meV and $M = 0.0$, $\lambda_E = -4.5$ meV; (c) and (g) $M = 9.0$ meV, $\lambda_E = 4.5$ meV and $M = -9.0$ meV, $\lambda_E = -4.5$ meV; and (d) and (h) $M = 9.0$ meV, $\lambda_E = 4.5$ meV and $M = -9.0$ meV, $\lambda_E = -4.5$ meV. The insets show the side view of a bilayer-graphene vdW spin valve configuration under consideration. The other parameters used in the calculations are $\gamma = 0.38$ eV and $U = 0.0$.

the spin degeneracy of the Dirac spectrum. The results are plotted in Figs. 2(c) and 2(g) and 2(d) and 2(h). From Eq. (3), we obtain analytically two extreme values, $E^{1,\varepsilon}_{I,\pm,s} = \varepsilon\sqrt{\frac{(\lambda^{\pm}_s)^2\gamma^2}{4(\lambda^{\pm}_s)^2+\gamma^2}}$ for $k_{I,\pm,s} = \sqrt{\frac{4(\lambda^{\pm}_s)^4+2(\lambda^{\pm}_s)^2\gamma^2}{4(\lambda^{\pm}_s)^2+\gamma^2}}$ and $E^{1,\varepsilon}_{II,\pm,s} = \varepsilon\lambda^{\pm}_s$ for $k_{II,\pm,s} = 0$, which divide the Dirac spectrum $E^{1,+}_{\pm,s}$ into two branches: regions I and II, defined by $E^{1,+}_{I,\pm,s} \leqslant E^{1,+}_{\pm,s} \leqslant E^{1,+}_{II,\pm,s}$ and $E^{1,+}_{\pm,s} > E^{1,+}_{II,\pm,s}$. Thus, the gaps between conduction and valence bands are given by $2E^{1,+}_{I,\pm,s}$ for $k = k_I$ and $2E^{1,+}_{II,\pm,s}$ for $k = k_{II}$, respectively. We also obtain analytically the spin splitting $E^{1,+}_{I,\pm,\uparrow} - E^{1,+}_{I,\pm,\downarrow}$ for $k = k_I$ and $E^{1,+}_{II,\pm,\uparrow} - E^{1,+}_{II,\pm,\downarrow}$ for $k = k_{II}$. For $\{M, \lambda_E\} \ll \gamma$, the differences in gaps and the spin splittings between $k = k_I$ and $k = k_{II}$ are negligible in the band structure, which can be seen in Fig. 2. (iii) Notice that the perfect switching of the spin polarization can be realized when switching the sign of M or λ_E in the mass term λ_s by properly tuning the gate voltage or AIF layer configuration. For device operations, a spin-dependent gap can be generated by the gate voltages, while the valley states are still degenerate. Thus, the on-site energy ϵ_{m_i} $(m = A, B; i = 1, 2)$ under the two AIF layers and the double-gate voltage coaction results in two important outcomes: opening a tunable band gap and realizing spin splitting. These properties of the energy spectra in BLG open venues for investigating perfect CAR.

Next, we propose bipolar setups to achieve nonlocal valley-entangled states via perfect CAR, with no contributions from the local AR and EC, in a BLG-based n-type vdW spin valve/SC/p-type vdW spin valve junction with asymmetric- and symmetric-gate configurations, as depicted in Figs. 3(a) and 3(b). For this study, we employ BLG to generate and detect the valley-entangled current by local band-gap engineering and proximity-induced superconductivity. The vdW spin valve region is composed of the dual-gate field-effect device. In order to reach the superconducting regime, here, we explore the effects of the superconducting proximity built around SC-BLG interfaces. Especially, the BLG flake encapsulated between a bottom and top h-BN is electrically contacted using edge contacts [63], which serve as source and drain electrodes for transport measurement. This type of electrode can also effectively suppress the intervalley scattering [64]. More specifically, the band gap and the carrier doping (Fermi energy) in the left and right vdW spin regions ($x \leqslant 0$ and $x \geqslant L$) can be controlled individually by tuning electrical gates, while the pair potential of the center superconducting region due to the proximity of the superconducting electrodes ($0 < x < L$) is taken to be constant. With this arrangement our model can be represented by $H_{Hyd}\Psi = E\Psi$. H_{Hyd} is the Dirac–Bogoliubov–de Gennes (DBdG) Hamiltonian in sublattice and particle-hole (Nambu) spaces first employed in

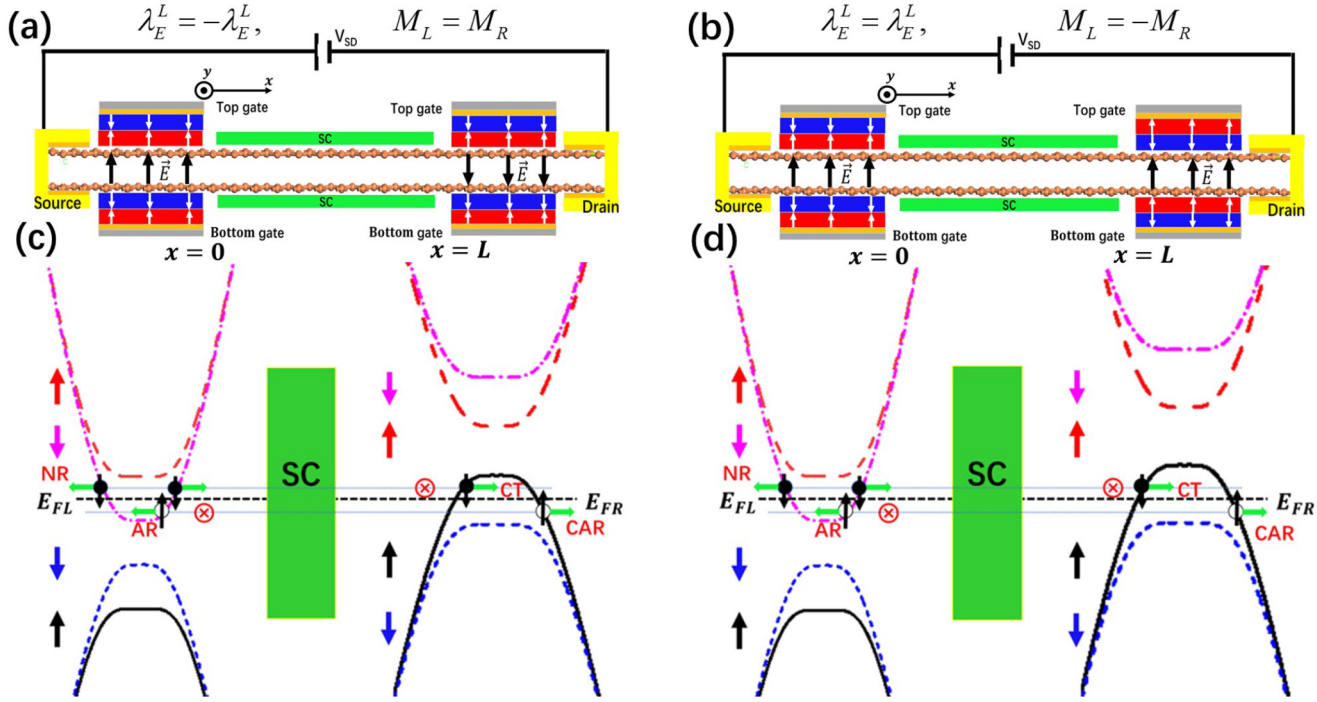

FIG. 3. (a) and (b) Schematic views of the devices used to realize pure valley-entangled states via CAR in the n-type vdW spin valve/SC/p-type vdW spin valve junction with asymmetric- and symmetric-gate configurations attached to the spin valve region, respectively. The junction resides in the x-y plane, and the interface is located at $x = 0$ and $x = L$. We assume that the superconductivity is induced in the BLG by means of the proximity effect. The BLG flake is electrically contacted using edge contacts. (c) and (d) Illustration of the mechanism of CAR in a gapped and spin-splitting dispersion. An incident electron residing in the lower conduction spin subband can be reflected as an electron or transmitted as a hole through the SC. Local AR and EC are, instead, completely blocked due to the large spin splitting in the conduction and valence bands.

Ref. [39], which can be defined as

$$H_{Hyd} = \begin{pmatrix} H_e - E_F & \Delta \\ \Delta^* & E_F - H_h \end{pmatrix}, \tag{4}$$

where

$$H_{e(h)} = \begin{pmatrix} \lambda_s^{\pm} & \hbar v_F \pi_{\mp} & 0 & 0 \\ \hbar v_F \pi_{\pm} & \lambda_s^{\pm} & \gamma & 0 \\ 0 & \gamma & \lambda_{-s}^{\mp} & \hbar v_F \pi_{\mp} \\ 0 & 0 & \hbar v_F \pi_{\pm} & \lambda_{-s}^{\mp} \end{pmatrix}. \tag{5}$$

Here, E is the excitation energy. $\Psi = (u \quad v)^T$ is the spinor. u and v are the four-component electron and hole wave functions, respectively, which have the form

$$\begin{aligned} u &= \left(u_{A_1,s,K} \quad u_{B_1,s,K} \quad u_{A_2,s,K} \quad u_{B_2,s,K}\right)^T, \\ v &= \left(v_{B_2,-s,K'} \quad v_{A_2,-s,K'} \quad v_{B_1,-s,K'} \quad v_{A_1,-s,K'}\right)^T, \end{aligned} \tag{6}$$

where T denotes the transpose. The Fermi energies E_F in the vdW spin valve regions and in the superconducting region are described by

$$E_F = \begin{cases} E_{FL}, & x \leqslant 0, \\ E_{FS}, & 0 < x < L \\ E_{FR}, & x \geqslant L, \end{cases} \tag{7}$$

where the Fermi energies E_{FL} and E_{FR} in the vdW spin valve regions include the electrostatic potentials U in Eq. (2). We have obtained a bipolar system by adjusting separately the electrostatic potentials U using dual-gate technology in vdW spin valve regions to have the same modulus U_0 but different signs, namely, $E_{FL} = -E_{FR} = U_0$. Moreover, E_{FS} in the superconducting region is strongly doped.

For simplicity, we also assume a steplike model for the spin-dependent potential $M(x)$, the potential difference $\lambda_E(x)$, and the pairing potential $\Delta(x)$,

$$\begin{aligned} M(x) &= M_L\Theta(-x) + M_R\Theta(x - L), \\ \lambda_E(x) &= \lambda_E^L\,\Theta(-x) + \lambda_E^R\,\Theta(x - L), \\ \Delta(x) &= \Delta_0\,\Theta(x)\Theta(L - x). \end{aligned} \tag{8}$$

Here, $\Theta(x)$ is the Heaviside step function.

To study the valley-entangled states in the BLG-based n-type vdW spin valve/SC/p-type vdW spin valve junction with edge-contact geometry, we analyze the scattering properties under the zero-temperature limit that an incoming electron from the left vdW spin valve region with excitation energy $E \geqslant 0$ and wave vector $\boldsymbol{k}_{L,e}^{\pm,s}$ at an angle α from the interface normal may experience by applying the scattering matrix approach [39,41,65]. Due to the translational invariance parallel to the interfaces, the scattering modes for the incident state with spin s and valley η have the form $\Psi_{\eta,s}^{\pm}(x, y) = \psi_{\eta,s}^{\pm}(x)e^{ik_y^{\pm,s}y}$. $k_y^{\pm,s}$ is a wave vector along the interface. In the following, we give the solutions of the wave functions $\psi_{\eta,s}^{\pm}(x)$

for three regions, which can be expressed as

$$\psi^{\pm}_{\eta,s}(x)=\begin{cases}\left[u^{\eta,s}_{L}\left(E,\pm k^{\pm,s}_{L,ex}\right)e^{\pm ik^{\pm,s}_{L,ex}x}+r^{\eta,s}_{N,\pm}u^{\eta,s}_{L}\left(E,\mp k^{\pm,s}_{L,ex}\right)e^{\mp ik^{\pm,s}_{L,ex}x}+r^{\eta,s}_{N\mp}u^{\eta,s}_{L}\left(E,\pm k^{\mp,s}_{L,ex}\right)e^{\pm ik^{\mp,s}_{L,ex}x}\right]\binom{1}{0}\\ +\left[r^{\eta,s}_{A,\pm}v^{\eta,s}_{L}\left(E,\pm k^{\pm,s}_{L,hx}\right)e^{\pm ik^{\pm,s}_{L,hx}x}+r^{\eta,s}_{A,\mp}v^{\eta,s}_{L}\left(E,\mp k^{\mp,s}_{L,hx}\right)e^{\mp ik^{\mp,s}_{L,hx}x}\right]\binom{0}{1}, \qquad x\leqslant 0,\\ a_1\phi_{M,e}\left(E,k^{+,s}_{M,ex}\right)e^{ik^{+,s}_{M,ex}x}+a_2\phi_{M,e}\left(E,-k^{+,s}_{M,ex}\right)e^{-ik^{+,s}_{M,ex}x}+a_3\phi_{M,e}\left(E,k^{-,s}_{M,ex}\right)e^{ik^{-,s}_{M,ex}x}\\ +a_4\phi_{M,e}\left(E,-k^{-,s}_{M,ex}\right)e^{-ik^{-,s}_{M,ex}x}+b_1\phi_{M,h}\left(E,k^{+,s}_{M,hx}\right)e^{ik^{+,s}_{M,hx}x}+b_2\phi_{M,h}\left(E,-k^{+,s}_{M,hx}\right)e^{-ik^{+,s}_{M,hx}x}\\ +b_3\phi_{M,h}\left(E,k^{-,s}_{M,hx}\right)e^{ik^{-,s}_{M,hx}x}+b_4\phi_{M,h}\left(E,-k^{-,s}_{M,hx}\right)e^{-ik^{-,s}_{M,hx}x}, \qquad 0<x<L,\\ \left[t^{\eta,s}_{EC,\pm}u^{\eta,s}_{R}\left(E,\mp k^{\pm,s}_{R,ex}\right)e^{\mp ik^{\pm,s}_{R,ex}x}+t^{\eta,s}_{EC\mp}u^{\eta,s}_{R}u^{s}_{R}\left(E,\pm k^{\mp,s}_{R,ex}\right)e^{\pm ik^{\mp,s}_{R,ex}x}\right]\binom{1}{0}+\left[t^{\eta,s}_{\mathrm{CA}\pm}v^{\eta,s}_{R}\left(E,\pm k^{\pm,s}_{R,ex}\right)e^{\pm ik^{\pm,s}_{R,hx}x}\right.\\ \left.+t^{\eta,s}_{\mathrm{CA},\mp}v^{\eta,s}_{R}\left(E,\mp k^{\mp,s}_{R,hx}\right)e^{\mp ik^{\mp,s}_{R,hx}x}\right]\binom{0}{1}, \qquad x\geqslant L,\end{cases} \tag{9}$$

where $r^{\eta,s}_{N,\tau}$, $r^{\eta,s}_{\mathrm{A},\tau}$, $t^{\eta,s}_{\mathrm{EC},\tau}$, and $t^{\eta,s}_{\mathrm{CA},\tau}$ are amplitudes of NR, AR, EC, and CAR, with $\tau=\pm$, while a_j and b_j, with $j\in\{1,2,3,4\}$, are the scattering amplitudes in the superconducting region. The upper $\pm$ sign in $\psi^{\pm}_{\eta,s}(x)$ labels two incident channels. $u^{\eta,s}_{L(R)}(E,\pm k^{\tau,s}_{L(R),ex})$ and $v^{\eta,s}_{L(R)}(E,\pm k^{\tau,s}_{L(R),hx})$ are the electron and hole eigenspinors of Eq. (4) in the vdW spin valve regions. $\phi_{M,e}(E,\pm k^{\tau,s}_{M,ex})$ and $\phi_{M,h}(E,\pm k^{\tau,s}_{M,hx})$ are the eigenspinors in the SC region. $k^{\tau,s}_{j,e(h)x}$, with $j=\{L,M,R\}$, are the wave vectors of the eigenstates. $k^{\tau,s}_{j,e(h)x}$ are chosen in such a way that the evanescent wave vanishes as $|x|\to\infty$. The explicit form of the eigenstates and the wave vectors in these three regions can be found in Appendix A.

Applying the continuity conditions of the wave functions at the boundaries $x=0$ and at $x=d$, the probability coefficients $R^{\eta,s}_{N,\tau}$, $R^{\eta,s}_{\mathrm{A},\tau}$, $T^{\eta,s}_{\mathrm{EC},\tau}$, and $T^{\eta,s}_{\mathrm{CA},\tau}$ can be obtained directly. For more details about the calculations, we refer the reader to Appendix B. Having obtained the above probability coefficients, we can investigate the nonlocal entangled Cooper pair splitting in our bipolar setups by analyzing the CAR coefficient $T^{\eta,s}_{\mathrm{CA},\tau}$ and the nonlocal differential conductance G_{CA} at zero temperature. G_{CA} can be written in terms of CAR coefficients,

$$G_{\mathrm{CA}}/G_0=\sum_{\tau,\eta,s}\left(\frac{G^{s}_{0,\tau}}{G_0}\right)\int_0^{\frac{\pi}{2}}d\alpha\left[T^{\eta,s}_{\mathrm{CA},\tau}(E,\alpha)+T^{\eta,s}_{\mathrm{CA},-\tau}(E,\alpha)\right]\cos\alpha. \tag{10}$$

Here, $E=eV_{SD}$ is the excitation energy, and α is the incident angle. $G_0=\sum_{\tau,s}G^{s}_{0,\tau}=\frac{e^2}{h}\sum_{\tau,s}\frac{w_y k^{\tau,s}_{L,e}}{\pi}$ denotes the differential conductance of the normal state. w_y is the width of the junction, and e is the electron charge. V_{SD} describes the bias voltage, as shown in Figs. 3(a) and 3(b). The results will be discussed in the next section.

III. RESULTS AND DISCUSSION

In this section, we discuss the results of calculations of the zero-temperature nonlocal conductance generated by perfect CAR, obtained by using Eq. (10). For definiteness, but without loss of generality, we assume a value of Δ_0= 1.5 meV for the proximity-induced gap in the SC region, which should be experimentally feasible [66]. To manifest the nonlocal transport, we also scale the length of the superconducting region L in units of the coherence length of the SC, $\xi_s=\frac{\hbar v_F}{\Delta_0}$. According to first-principles results [49], we set the typical value of the AIF configuration-induced $M=4.5$ meV. Throughout the paper, the other energies are in units of Δ_0= 1.5 meV.

For conciseness, we take the n-SC-p bipolar junctions in edge-contact geometry [see Figs. 3(a) and 3(b)], in which the single-channel mechanism is realized in two distinct setups of the vdW spin valve/SC/vdW spin valve junction, namely, the n-SC-p junction with the asymmetric-gate configuration ($\lambda^L_E\lambda^R_E<0$ and $M_LM_R>0$) and the symmetric-gate configuration ($\lambda^L_E\lambda^R_E>0$ and $M_LM_R<0$). In these setups, we find that only an electron channel residing in the $s=\downarrow$ conduction subband is allowed in the left vdW spin valve region, whereas only a purely $s=\uparrow$ polarized valence hole channel is allowed in the other one. Moreover, to enter the superconducting condensate, an electron needs a partner of the opposite spin and different valley index. As a result, in the reflected region $x\leqslant 0$, local AR is no longer possible because no opposite spin electrons are available below the Fermi energy for local AR. In the transmitted region $x\geqslant L$, EC is also completely suppressed because of the spin conservation, which prevents the electron from tunneling into the opposite-spin valence subband. These mean that the scattering processes of local NR and perfect CAR are the only ones physically allowed. Moreover, we find that the spin degeneracy is lifted near the Fermi energy, while degeneracy remains in valley states in each case, as shown in Figs. 3(c) and 3(d). Thus, we can explore perfect CAR for the nonlocal valley-entangled Cooper pair splitting, which is useful for nonlocal Einstein-Podolsky-Rosen pairs.

In the following numerical calculation, we further fix $\gamma=\frac{760}{3}\Delta_0$, $U_0=3\Delta_0$, $|\lambda^j_E|=6\Delta_0$, $|M_j|=3\Delta_0$ $(j=L,R)$ and set the bias voltage to $V_{SD}=\frac{E}{e}$, with $E=\frac{2}{3}\Delta_0$. Since the interlayer coupling γ is larger than other energies, $\gamma\gg\{|\lambda^i_E|,|M_i|,U_0\}$, the longitudinal momenta $k^{-,\downarrow}_{j,ex}$ and $k^{-,\downarrow}_{j,hx}$ in Eq. (9) become imaginary momenta. Thus, the incident channel $\psi^{-}_{\eta,\downarrow}(x)$ is an evanescent mode which decays away from the interface with imaginary momenta. Below, we neglect the $\psi^{-}_{\eta,\downarrow}(x)$ channel and just analyze the real solutions of $k^{+,\downarrow}_{j,ex}$ corresponding to the propagating channel, namely, $\psi^{+}_{\eta,\downarrow}(x)$. The identity of particle conservation in Appendix B becomes $R^{\eta,\downarrow}_{N,+}+R^{\eta,\downarrow}_{A,+}+T^{\eta,\downarrow}_{EC,+}+T^{\eta,\downarrow}_{\mathrm{CA},+}=1$.

To see how the nonlocal valley-entanglement transport can be obtained via perfect CAR, we focus on NR and perfect CAR transport phenomena. In Fig. 4, we calculate and present the probabilities of the four processes as a function of the incident angle α. In Fig. 4, the numerical results show that

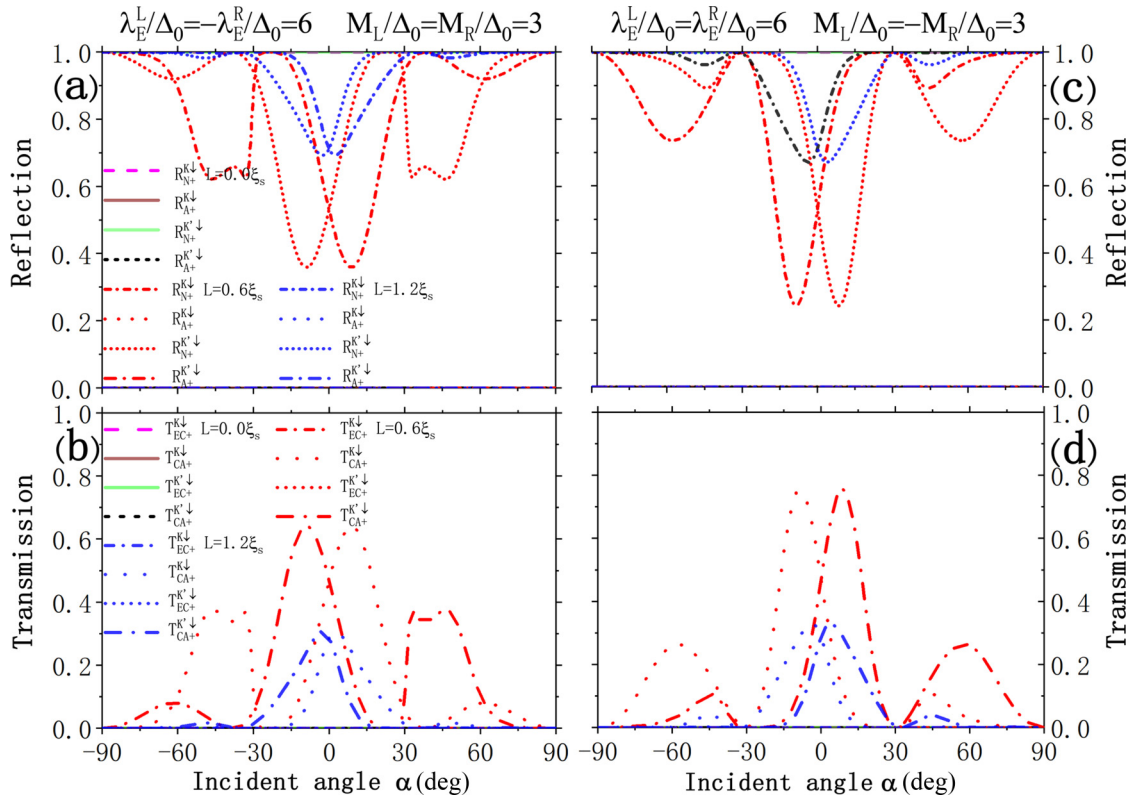

FIG. 4. Angular dependence of the probabilities of the four processes for different values of the length L of the SC region. The probabilities of reflection and transmission for the n-SC-p junction in edge-contact geometry with (a) and (b) the asymmetric-gate configuration [$\lambda_E^L\lambda_E^R < 0$ and $M_L M_R > 0$] and (c) and (d) the symmetric-gate configuration [$\lambda_E^L\lambda_E^R > 0$ and $M_L M_R < 0$]. $V_{SD} = \frac{E}{e}$, with $E = \frac{2}{3}\Delta_0$, is the voltage bias across the junction. Here, we have used $\gamma = \frac{760}{3}\Delta_0$, $U_0 = 3\Delta_0$, and $E_{FS} = \frac{100}{3}\Delta$ for all plots.

the processes of local AR and EC are completely suppressed, $R_{A,+}^{\eta,\downarrow} = T_{EC,+}^{\eta,\downarrow} = 0$, which is in agreement with the previous qualitatively physical explanation. In the limit $L \to 0$, it is seen that the CAR process is completely absent due to the absence of superconductivity: $T_{\mathrm{CA},+}^{\eta,\downarrow} = 0$. Thus, the NR is perfect with $R_{N,+}^{\eta,\downarrow} = 1$ due to the particle conservation. However, at intermediate length scales $L = 0.6\xi_s$, a large perfect CAR can occur in addition to normal reflection for incident angle α. As the length L is longer than the superconducting coherence length $L = 1.2\xi_s$, we emphasize that the CAR probability still persists, while the amplitude of perfect CAR is suppressed. This comparison is shown in Figs. 4(b) and 4(d). When the coherence length L is finite, we also note that NR and CAR behaviors exhibit an oscillation behavior. Moreover, the asymmetry of NR and CAR coefficients between positive and negative angles is reversed if the valley state of the incident quasiparticle is reversed, i.e.,

$$R_{N,+}^{K,\downarrow}(\alpha) = R_{N,+}^{K',\downarrow}(-\alpha),\ T_{\mathrm{CA},+}^{K,\downarrow}(\alpha) = T_{\mathrm{CA},+}^{K',\downarrow}(-\alpha). \tag{11}$$

This result can be guaranteed by the following symmetry operation of the DBdG equation [see Eq.(4)]:

$$SH_{Hyd}(\pi^{\pm})S^{-1} = H_{Hyd}(-\pi^{\pm}), \tag{12}$$

where $S = P_y C_\eta$ consists of the transformation ($P_y : y \to -y$) and the inversion of the valley state ($C_\eta : \eta \to -\eta$). Consequently, it follows from the boundary conditions [see Eqs. (B1) and (B2) in Appendix B] that the scattering coefficients for $\pi^{\pm}$ equal the one for $-\pi^{\pm}$.

In Fig. 5, we show results for the perfect CAR conductance G_{CA} as a function of the superconducting BLG Fermi energy E_{FS} for several values of L. In both cases, the magnitude of the CAR conductance shows a strenuous Fabry-Pérot oscillatory dependence on Fermi energy E_{FS} for short junctions $L = 0.2\xi_s$ (black dotted line in Fig. 5). Upon increasing the junction length L [see red and blue dotted lines in Fig. 5(a)], the CAR conductance is severely damped, and the Fabry-Pérot oscillating behavior is not pronounced, while the frequency of the G_{CA} oscillation is increased. As shown by the red and blue dotted lines in Fig. 5(b), we note that the main results do not change qualitatively, while the pattern of CAR conductance oscillations is still a more prominent feature for large values of E_{FS}, and one noteworthy thing is that the oscillation amplitudes for the n-SC-p junction in edge-contact geometry with the asymmetric-gate configuration ($\lambda_E^L\lambda_E^R < 0$ and $M_L M_R > 0$) are 10 times larger than those in the case with the symmetric-gate configuration ($\lambda_E^L\lambda_E^R > 0$ and $M_L M_R < 0$). Our findings suggest that the proposed device can act as an on-off switch that operates the nonlocal valley-entangled Cooper pair splitting.

Physically, the oscillatory behavior arises from the interference effect between electronlike and holelike quasiparticles in the SC region. For $E < \Delta_0$, the wave vector $k_{M,e(h)x}^{+,\downarrow} = \mathrm{Re}[\kappa_{M,e(h)x}^{+,\downarrow}] + (-)i\mathrm{Im}[\kappa_{M,e(h)x}^{+,\downarrow}]$ [for more informa-

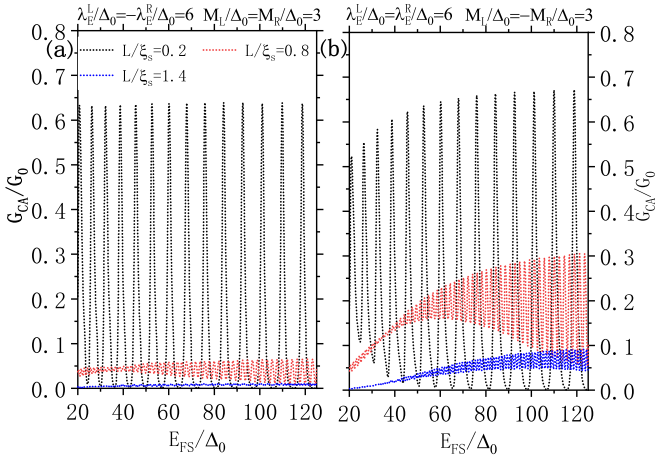

FIG. 5. Dependence of the CAR conductance on the magnitude of the Fermi energy in SC region E_{FS} for the n-SC-p junction in edge-contact geometry with (a) the asymmetric-gate configuration ($\lambda_E^L\lambda_E^R < 0$ and $M_L M_R > 0$) and (b) the symmetric-gate configuration ($\lambda_E^L\lambda_E^R > 0$ and $M_L M_R < 0$). The three lines correspond to different lengths of the SC region: $L = 0.2\xi_s$ (black dotted line), $L = 0.8\xi_s$ (red dotted line), and $L = 1.4\xi_s$ (blue dotted line). Here, $E = \frac{2}{3}\Delta_0$, and other parameters are the same as those described in the caption of Fig. 4.

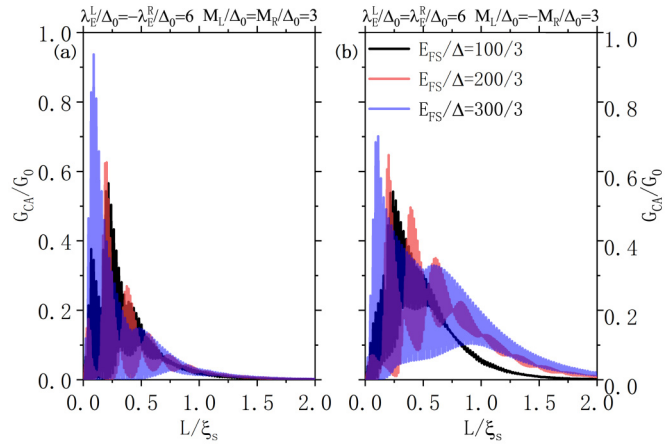

FIG. 6. Plots of the conductance for CAR processes $G_{\rm CA}/G_0$ versus the length of the SC region for the n-SC-p junction in edge-contact geometry with (a) the asymmetric-gate configuration ($\lambda_E^L\lambda_E^R < 0$ and $M_L M_R > 0$) and (b) the symmetric-gate configuration ($\lambda_E^L\lambda_E^R > 0$ and $M_L M_R < 0$) for three different Fermi energies E_{FS} in the SC region. Here, $E = \frac{2}{3}\Delta_0$, and other parameters are the same as those described in the caption of Fig. 4.

tion on $\kappa^{+,\downarrow}_{M,e(h)x}$, see Eq. (A8) in Appendix A] in the SC region is composed of a propagating term, $\mathrm{Re}[\kappa^{+,\downarrow}_{M,e(h)x}]$, and a damping term, $\mathrm{Im}[\kappa^{+,\downarrow}_{M,e(h)x}]$. The oscillation period is determined by the resonant condition $(\mathrm{Re}[\kappa^{+,\downarrow}_{M,ex}] - \mathrm{Re}[\kappa^{+,\downarrow}_{M,hx}])L = 2n\pi$. $\kappa^{+,\downarrow}_{M,ex}$ can be modified by tuning directly the bias voltage $V_{SD} = \frac{E}{e}$ and the doping of E_{FS} in the SC region. Increasing E_{FS} thus leads to a stronger oscillation. With increasing L, the imaginary term $\mathrm{Im}[\kappa^{+,\downarrow}_{M,e(h)x}]L$ becomes larger. This results in a strongly reduced CAR conductance. The increase in L rapidly enlarges $n = \frac{\mathrm{Re}[\kappa^{+,\downarrow}_{M,e(h)x}]L}{2\pi}$. Hence, we see clearly that $G_{\rm CA}$ exhibits a rapid oscillation. The most interesting aspect is that tuning the Fermi energy of the superconducting BLG offers a useful parameter to control the valley-entanglement transport.

Next, we calculate the cross conductance $G_{\rm CA}$ as a function of the SC length L for three different Fermi energies E_{FS} in the SC region, as shown in Fig. 6. The behavior of $G_{\rm CA}$ depends sensitively on the length L compared to the coherence length ξ_s. In the limit $L \to 0$, $G_{\rm CA}$ vanishes due to the absence of superconductivity. For small length $L < \xi_s$, the increase in L surprisingly enhances $G_{\rm CA}$ until it reaches its resonant peak, when $L \approx \frac{1}{4}\xi_s$, but once $L > \frac{1}{4}\xi_s$, the maximum value that $G_{\rm CA}$ can reach starts to decrease with L. In the case $L > \xi_s$, the large $G_{\rm CA}$ persists in the junction and drops to zero as soon as $L \gg \xi_s$. This is a direct consequence of the wave vectors $k^{+,\downarrow}_{M,e(h)x}$ in the SC region, which have finite real and imaginary parts. When $L \approx \frac{1}{4}\xi_s$, the real part $\mathrm{Re}[\kappa^{+,\downarrow}_{M,e(h)x}]$ becomes dominant, which brings trigonometric functions into the formula, and this causes the fast oscillations. Far away from the coherent length ξ_s, the imaginary part $\mathrm{Im}[\kappa^{+,\downarrow}_{M,e(h)x}]$ plays a dominant role, which causes the tunneling across SC to exponentially decay.

In Fig. 7, G_{EC} and $G_{\rm CA}$ as a function of the bias voltage $V_{SD} = \frac{E}{e}$ are plotted for different values of Fermi energy E_{FS} with $L = 0.5\xi_s$ [Figs. 7(a) and 7(b)] and junction length L with $E_{FS}/\Delta_0 = 100/3$ [Figs. 7(c) and 7(d)]. Notice that G_{EC} can be calculated just by replacing $T_{\rm CA}$ in Eq. (10) with T_{EC}. As seen in Fig. 7, the CAR conductance $G_{\rm CA}$ is favored, while EC conductance G_{EC} is vanishing. We can qualitatively explain this result as follows. In Figs. 3(c) and 3(d), when a gate voltage is applied, the spin degeneracy in the left and right vdW spin valve regions is lifted. By using Eq. (3), we can find that the analytical expressions of the split energy for the lowest conduction band and the highest valence band are $E^{1,+}_{\pm,s} = \sqrt{\frac{(\lambda_s^{\pm})^2\gamma^2}{4(\lambda_s^{\pm})^2+\gamma^2}} - U_0$ and $E^{1,+}_{\pm,s} = U_0 - \sqrt{\frac{(\lambda_s^{\pm})^2\gamma^2}{4(\lambda_s^{\pm})^2+\gamma^2}}$, respectively. For $\gamma \gg \lambda_s$, the onset of the incident-electron energy contributing to the single-channel transport in the left vdW spin valve region is from $|\lambda^+_\downarrow| - U_0$ to $|\lambda^-_\downarrow| - U_0$, and the opposite spin electron channels below the Fermi energy, which are allowed only in right vdW spin valve region, are from $U_0 - |\lambda^+_\uparrow|$ to $U_0 - |\lambda^-_\uparrow|$. Thus, the incident-energy windows which are the key to obtaining the perfect CAR process are from $E/\Delta_0 = 0$ to $E/\Delta_0 = 6$ when $\lambda_E^L = 6\Delta_0$, $M_L = 3\Delta_0$, and $U_0 = 3\Delta_0$ are fixed, which is out of the superconducting gap Δ_0 range. In the perfect CAR process, we emphasize here that the SC plays a role in converting electrons to holes. It is not crucial that the bias voltage must be shifted into the superconducting gap. The key issue is that the single-electron channel and the single-hole channel must be realized in the two leads. Moreover, it is seen that the $G_{\rm CA}$ resonances are in the limit $E \to 0$. In this case, the incident (outgoing) energy lies closer to the bottom (top) of the conduction (valance) band. This means that EC and local AR process are completely blocked and only NR and perfect CAR are possible because the spectrum is gapped on the two leads. Still, it should be noted that we find that $G_{\rm CA}$

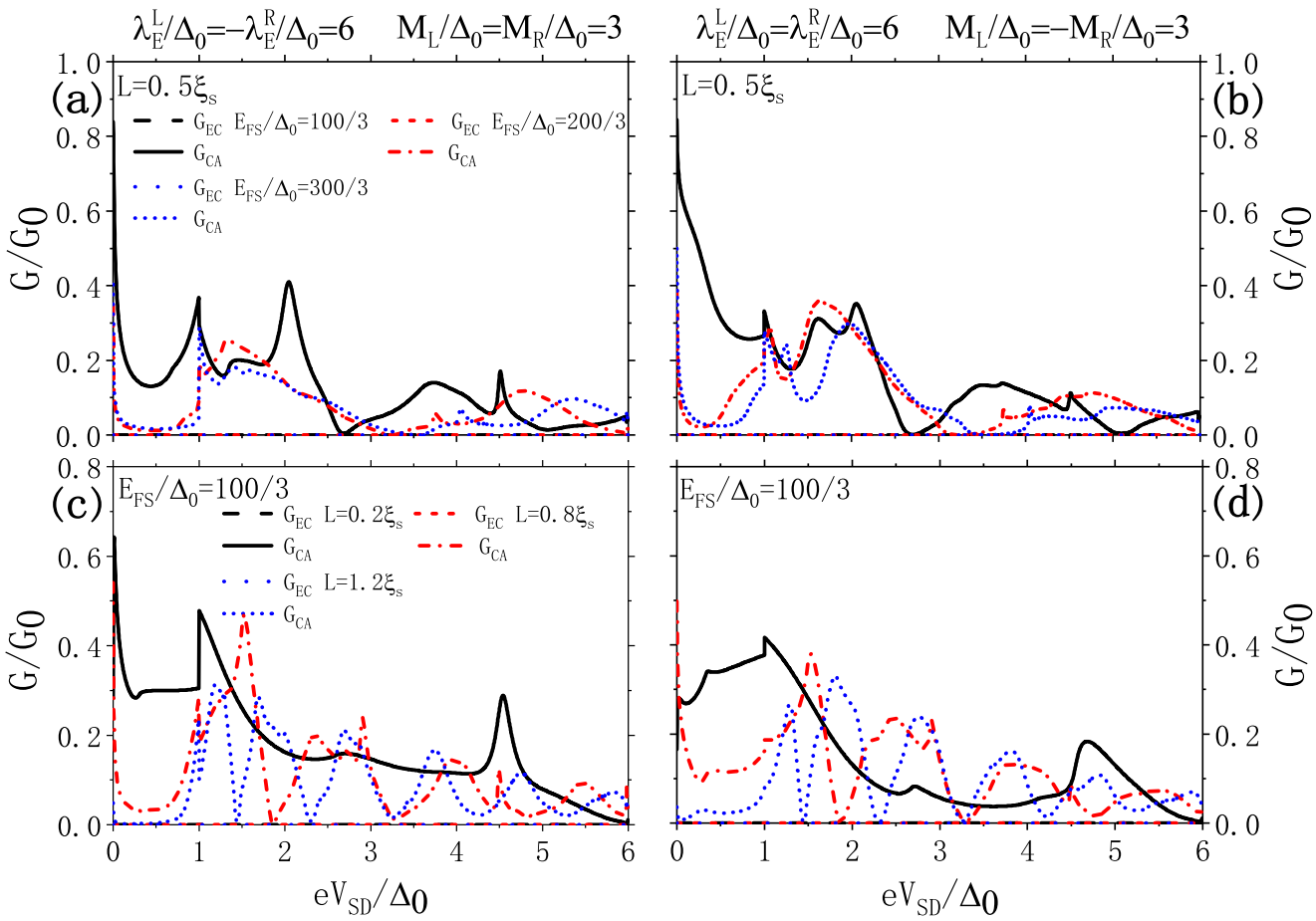

FIG. 7. Charge conductance of the EC and CAR processes as a function of the bias voltage $V_{SD} = \frac{E}{e}$ for different values of (a) and (b) the Fermi energy E_{FS} with $L = 0.5\xi_s$ and (c) and (d) junction length L with $E_{FS}/\Delta_0 = 100/3$. In these plots $\gamma = \frac{760}{3}\Delta_0$ and $U_0 = 3\Delta_0$.

has a distinct peak at $E = \Delta_0$ independent of the Fermi energy E_{FS} and junction length L. Increasing E further, we find that the conductance $G_{\rm CA}$ oscillates due to the quasiparticle interferences inside the superconducting region. Interestingly, $G_{\rm CA}$ minima are near zero. This suggests that the nonlocal valley-entanglement effect can be completely switched off by a fine tuning of the bias voltage.

Last, let us have a brief discussion of the experimental feasibility of our physical model. First, our device requires the intervalley scattering in BLG to be suppressed significantly to achieve the valley-entangled electrons via CAR. To overcome this obstacle, we set the orientation of the BLG nanoribbons with the effective zigzag edge and sandwich the BLG between two thin h-BN layers, which can eliminate the intervalley scattering caused by the sharp defects, substrate roughness, and armchair edge [64,67]. In addition, the conducting channel is established inside the BLG away from the atomically rugged edge to greatly reduce the valley-mixing scattering. Second, the main results discussed above are proposed to be within the superconducting coherence length. The temperature has to be low compared to the critical temperatures T_c of the SC. For instance, in $NbSe_2$, we have $T_c \sim 14$ K [66]. Recently, it was shown that the insulating ferromagnet CrI_3 remains ferromagnetic up to 45 K [68]. Thus, the experiment at a low temperature is necessary. Furthermore, we point out that the valley-entangled ballistic beam splitter via the CAR mechanism proposed here could be detected by testing the expectation value of the entanglement witness operator [69]. Finally, we stress that our results are also applicable to silicene, MoS_2, and other group-VI dichalcogenides in the presence of the interlayer electric field and antiferromagnetic exchange fields.

IV. CONCLUSION

In conclusion, we have theoretically studied the quantum transport properties in the n-type vdW spin valve/SC/p-type vdW spin valve junction with edge-contact geometry. We have proposed two different setups, in which splitting a valley-entanglement Cooper pair into two separate leads via perfect CAR can be created by manipulating the top and bottom gates in the vdW spin valve regions. We also calculate the differential conductance $G_{\rm CA}$, which provides a direct measurement of the perfect CAR. We find that it is possible to control perfect CAR by the doping of SC, the junction length, and the bias voltage. In particular, we have shown that $G_{\rm CA}$ exhibits a large oscillation behavior. Thus, our proposed devices can be used to realize rapid on-off switching of the nonlocal valley-entanglement state. Finally, we expect that the production of valley-entangled electron pairs using these setups can be guided by our analysis, which can also provide useful additions to future experiments on valleytronics [70].

ACKNOWLEDGMENTS

This work is supported by the Special Foundation for Theoretical Physics Research Program of China under Grant No. 11747035, the Scientific Research Foundation of Yancheng Institute of Technology under Grant No. XJ201743, and the National Natural Science Foundation of China under Grants No. 11604195, No. 11704324, and No. 11804290.

APPENDIX A: SOLUTIONS OF THE DBdG EQUATION

In this Appendix, we briefly introduce the plane wave solutions of DBdG equation [see Eq. (4)] for electrons and holes in three regions of the bilayer graphene system. These solutions for the left vdW spin valve region take the following form:

$$u_L^{\eta,s}\left(E,\pm k_{L,ex}^{\tau,s}\right)e^{\pm ik_{L,ex}^{\tau,s}x}=\frac{1}{N_{L,e}^{\tau,s}}\begin{pmatrix}E_{L,+}\left(\Gamma_{L,e}^{\tau,s}+\gamma^2\right)+\lambda_{L,s}^{+}\left[\Gamma_{L,e}^{\tau,s}-4\left(k_{L,e}^{\tau,s}\right)^2+\gamma^2\right]\\ \pm 2\pi_{\pm,L,ex}^{\tau,\eta,s}\left[\left(k_{L,e}^{\tau}\right)^2-\left(E_{L,+}+\lambda_{L,s}^{+}\right)^2\right]\\ \mp 2\gamma\pi_{\pm,L,ex}^{\tau,\eta,s}\left(E_{L,+}+\lambda_{L,s}^{+}\right)\\ -2\gamma\left(\pi_{\pm,L,ex}^{\tau,s}\right)^2\end{pmatrix}e^{\pm ik_{L,ex}^{\tau,s}x},$$

$$v_L^{\eta,s}\left(E,\pm k_{L,hx}^{\tau,s}\right)e^{\pm ik_{L,hx}^{\tau}x}=\frac{1}{N_{L,h}^{\tau,s}}\begin{pmatrix}E_{L,-}\left(\Gamma_{L,h}^{\tau,s}+\gamma^2\right)-\lambda_{L,-s}^{+}\left[\Gamma_{\mathrm{L},h}^{\tau,s}-4\left(k_{L,h}^{\tau}\right)^2+\gamma^2\right]\\ \pm 2\pi_{\mp,L,hx}^{\tau,\eta,s}\left[\left(k_{L,h}^{\tau,s}\right)^2-\left(E_{L,-}-\lambda_{L,-s}^{+}\right)^2\right]\\ \mp 2\gamma\pi_{\mp,L,hx}^{\tau,\eta,s}\left(E_{L,-}-\lambda_{L,-s}^{+}\right)\\ -2\gamma\left(\pi_{\mp,L,hx}^{\tau,s}\right)^2\end{pmatrix}e^{\pm ik_{L,hx}^{\tau,s}x},\tag{A1}$$

with

$$\Gamma_{L,e}^{\tau,s}=\sqrt{\gamma^4+4\left(k_{L,e}^{\tau,s}\right)^2[(2\lambda_{L,s}^{+})^2+\gamma^2]},\quad \Gamma_{L,h}^{\tau,s}=\sqrt{\gamma^4+4\left(k_{\mathrm{L},h}^{\tau,s}\right)^2[(2\lambda_{L,-s}^{+})^2+\gamma^2]},\tag{A2}$$

where $\tau=\pm$ and $E_{L,\pm}=E_{FL}\pm E$.

These solutions in the right region are given as

$$u_R^{\eta,s}\left(E,\pm k_{R,ex}^{\tau,s}\right)e^{\pm ik_{R,ex}^{\tau,s}x}=\frac{1}{N_{R,e}^{\tau,s}}\begin{pmatrix}-E_{R,-}\left(\Gamma_{R,e}^{\tau,s}+\gamma^2\right)+\lambda_{R,s}^{+}\left[\Gamma_{R,e}^{\tau,s}-4\left(k_{R,e}^{\tau,s}\right)^2+\gamma^2\right]\\ \pm 2\pi_{\pm,R,ex}^{\tau,\eta,s}\left[\left(k_{R,e}^{\tau,s}\right)^2+\left(E_{R,-}-\lambda_{R,s}^{+}\right)^2\right]\\ \pm 2\gamma\pi_{\pm,R,ex}^{\tau,\eta,s}\left(E_{R,-}-\lambda_{R,s}^{+}\right)\\ -2\gamma\left(\pi_{\pm,R,ex}^{\tau,\eta,s}\right)^2\end{pmatrix}e^{\pm ik_{R,ex}^{\tau,s}x},$$

$$v_R^{\eta,s}\left(E,\pm k_{L,hx}^{\tau,s}\right)e^{\pm ik_{R,hx}^{\tau,s}x}=\frac{1}{N_{R,h}^{\tau,s}}\begin{pmatrix}-E_{R,+}\left(\Gamma_{R,h}^{\tau,s}+\gamma^2\right)-\lambda_{R,-s}^{+}\left[\Gamma_{R,h}^{\tau,s}-4\left(k_{R,h}^{\tau,s}\right)^2+\gamma^2\right]\\ \pm 2\pi_{\mp,R,hx}^{\tau,\eta,s}\left[\left(k_{R,h}^{\tau,s}\right)^2-\left(E_{R,+}+\lambda_{R,-s}^{+}\right)^2\right]\\ \pm 2\gamma\pi_{\mp,R,hx}^{\tau,\eta,s}\left(E_{R,+}+\lambda_{R,-s}^{+}\right)\\ -2\gamma\left(\pi_{\mp,R,hx}^{\tau,\eta,s}\right)^2\end{pmatrix}e^{\pm ik_{R,hx}^{\tau,s}x},\tag{A3}$$

where

$$\Gamma_{R,e}^{\tau,s}=\sqrt{\gamma^4+4\left(k_{R,e}^{\tau,s}\right)^2[(2\lambda_{R,s}^{+})^2+\gamma^2]},\quad \Gamma_{R,h}^{\tau,s}=\sqrt{\gamma^4+4\left(k_{R,h}^{\tau,s}\right)^2[(2\lambda_{R,-s}^{+})^2+\gamma^2]},\tag{A4}$$

with $E_{R,\pm}=E_{FR}\pm E$. Above, N is the normalization factor where $u^{\dagger}u=1$ and $v^{\dagger}v=1$.

Inside the SC, the solutions of the DBdG equation are two states of the form

$$\phi_{M,e}\left(E,\pm k_{M,ex}^{\tau,s}\right)e^{\pm ik_{M,ex}^{\tau,s}x}=\begin{pmatrix}\mp i\pi_{\mp,M,ex}^{\tau,\eta,s}\left(E_{FS}-E+\Gamma_{M,e}^{\tau,s}\right)\\ \times i\left[\left(k_{M,e}^{\tau,s}\right)^2+\Gamma_{M,e}^{\tau,s}(E_{FS}-E-\gamma)\right]\\ \times\ i\left[\left(k_{M,e}^{\tau,s}\right)^2+\Gamma_{M,e}^{\tau,s}(E_{FS}-E-\gamma)\right]\\ \mp i\pi_{\pm,M,ex}^{\tau,\eta,s}\left(E_{FS}-E+\Gamma_{M,e}^{\tau,s}\right)\\ \pm i\pi_{\pm,M,ex}^{\tau,\eta,s}\Delta^{*}\\ -i\Gamma_{M,e}^{\tau,s}\Delta^{*}\\ -i\Gamma_{M,e}^{\tau,s}\Delta^{*}\\ \pm i\pi_{\mp,M,ex}^{\tau,\eta,s}\Delta^{*}\end{pmatrix}e^{\pm ik_{M,ex}^{\tau,s}x},$$

$$\phi_{M,h}\left(E,\pm k_{M,hx}^{\tau,s}\right)e^{\pm ik_{M,hx}^{\tau,s}x}=\begin{pmatrix}\mp i\pi_{\mp,M,hx}^{\tau,\eta,s}\left(E_{FS}+E-\Gamma_{M,h}^{\tau,s}\right)\\ \times i\left[\left(k_{M,h}^{\tau,s}\right)^2-\Gamma_{M,h}^{\tau,s}(E_{FS}+E+\gamma)\right]\\ -i\left[\left(k_{M,h}^{\tau,s}\right)^2-\Gamma_{M,h}^{\tau,s}(E_{FS}+E+\gamma)\right]\\ \pm i\pi_{\pm,M,hx}^{\tau,\eta,s}\left(E_{FS}+E-\Gamma_{M,h}^{\tau,s}\right)\\ \mp i\pi_{\pm,M,hx}^{\tau,\eta,s}\Delta^*\\ -i\Gamma_{M,h}^{\tau,s}\Delta^*\\ \times i\Gamma_{M,h}^{\tau,s}\Delta^*\\ \pm i\pi_{\mp,M,hx}^{\tau,\eta,s}\Delta^*\end{pmatrix}e^{\pm ik_{M,hx}^{\tau,s}x},\tag{A5}$$

where we have introduced the following notation:

$$\Gamma_{M,e}^{\tau,s}=\sqrt{\left(k_{M,e}^{\tau,s}\right)^2+\frac{\gamma^2}{4}}-\frac{\gamma}{2},\quad \Gamma_{M,h}^{\tau,s}=\sqrt{\left(k_{M,h}^{\tau,s}\right)^2+\frac{\gamma^2}{4}}-\frac{\gamma}{2}.\tag{A6}$$

Above, $\pi_{\pm,j,e(h)x}^{\tau,\eta,s}=\eta k_{j,e(h)x}^{\tau,s}\pm ik_y^{\tau,s}$, and $(k_{j,e(h)}^{\tau,s})^2=(k_{j,e(h)x}^{\tau,s})^2+(k_y^{\tau,s})^2$. Here, $k_{j,e(h)x}^{\tau,s}$, with $j=\{L,M,R\}$) are the wave vectors. To ensure that the evanescent wave decays exponentially as $|x|\to\infty$, the wave vectors can be written as

$$\begin{aligned}k_{L,e(h)x}^{\tau,s}&=\mathrm{Re}\left[\kappa_{L,e(h)x}^{\tau,s}\right]+(-)i\mathrm{Im}\left[\kappa_{L,e(h)x}^{\tau,s}\right],\\ k_{M,e(h)x}^{\tau,s}&=\mathrm{Re}\left[\kappa_{M,e(h)x}^{\tau,s}\right]+(-)i\mathrm{Im}\left[\kappa_{M,e(h)x}^{\tau,s}\right],\\ k_{R,e(h)x}^{\tau,s}&=\mathrm{Re}\left[\kappa_{R,e(h)x}^{\tau}\right]-(+)i\mathrm{Im}\left[\kappa_{R,e(h)x}^{\tau,s}\right],\end{aligned}\tag{A7}$$

with

$$\begin{aligned}\kappa_{L,ex}^{\tau,s}&=\sqrt{(E_{L,+})^2-\left(k_y^{\tau,s}\right)^2+(\lambda_{L,s}^{+})^2+\tau\sqrt{(2E_{L,+}\lambda_{L,s}^{+})^2+[(E_{L,+})^2-(\lambda_{L,s}^{+})^2]\gamma^2}},\\ \kappa_{L,hx}^{\tau,s}&=\sqrt{(E_{L,-})^2-\left(k_y^{\tau,s}\right)^2+(\lambda_{L,-s}^{+})^2+\tau\sqrt{(2E_{L,-}\lambda_{L,-s}^{+})^2+[(E_{L,-})^2-(\lambda_{L,-s}^{+})^2]\gamma^2}},\\ \kappa_{R,ex}^{\tau,s}&=\sqrt{(E_{R,-})^2-\left(k_y^{\tau,s}\right)^2+(\lambda_{R,s}^{+})^2+\tau\sqrt{(2E_{R,-}\lambda_{R,s}^{+})^2+[(E_{R,-})^2-(\lambda_{R,s}^{+})^2]\gamma^2}},\\ \kappa_{R,hx}^{\tau,s}&=\sqrt{(E_{R,+})^2-\left(k_y^{\tau,s}\right)^2+(\lambda_{R,-s}^{+})^2+\tau\sqrt{(2E_{R,+}\lambda_{R,-s}^{+})^2+[(E_{R,+})^2-(\lambda_{R,-s}^{+})^2]\gamma^2}},\\ \kappa_{M,ex}^{\tau,s}&=\sqrt{E^2-\left(k_y^{\tau,s}\right)^2+E_{FS}(E_{FS}-\gamma)-\Delta\Delta^*+\tau\sqrt{(2E_{FS}-\gamma)^2(E^2-\Delta\Delta^*)}},\\ \kappa_{M,hx}^{\tau,s}&=\sqrt{E^2-\left(k_y^{\tau,s}\right)^2+E_{FS}(E_{FS}+\gamma)-\Delta\Delta^*+\tau\sqrt{(2E_{FS}+\gamma)^2(E^2-\Delta\Delta^*)}},\end{aligned}\tag{A8}$$

where $k_y^{\tau,s}=\sqrt{(E_{L,+})^2-(k_y^{\tau,s})^2+(\lambda_{L,s}^{+})^2+\tau\sqrt{(2E_{L,+}\lambda_{L,s}^{+})^2+[(E_{L,+})^2-(\lambda_{L,s}^{+})^2]\gamma^2}}\sin\alpha$ is the transverse wave vector along the interface. α is the angle of incidence relative to the x direction.

APPENDIX B: THE BOUNDARY CONDITIONS

In this Appendix we show how to get the scattering amplitudes of the various scattering processes [Eq. (9)] by imposing the continuity of the wave function at $x=0$ and $x=L$. Then we can obtain the following sets of equations for the reflection and transmission amplitudes:

$$\begin{aligned}&\left[u_L^{\eta,s}\left(E,\pm k_{L,ex}^{\pm,s}\right)+r_{N,\pm}^{\eta,s}u_L^{\eta,s}\left(E,\mp k_{L,ex}^{\pm,s}\right)+r_{N\mp}^{\eta,s}u_L^{\eta,s}\left(E,\pm k_{L,ex}^{\mp,s}\right)\right]\binom{1}{0}+\left[r_{A,\pm}^{\eta,s}v_L^{\eta,s}\left(E,\pm k_{L,hx}^{\pm,s}\right)+r_{A,\mp}^{\eta,s}v_L^{\eta,s}\left(E,\mp k_{L,hx}^{\mp,s}\right)\right]\binom{0}{1}\\ &\quad=a_1\phi_{M,e}\left(E,k_{M,ex}^{+,s}\right)+a_2\phi_{M,e}\left(E,-k_{M,ex}^{+,s}\right)+a_3\phi_{M,e}\left(E,k_{M,ex}^{-,s}\right)+a_4\phi_{M,e}\left(E,-k_{M,ex}^{-,s}\right)+b_1\phi_{M,h}\left(E,k_{M,hx}^{+,s}\right)+b_2\phi_{M,h}\left(E,-k_{M,hx}^{+,s}\right)\\ &\qquad+b_3\phi_{M,h}\left(E,k_{M,hx}^{-,s}\right)+b_4\phi_{M,h}\left(E,-k_{M,hx}^{-,s}\right)\end{aligned}\tag{B1}$$

and

$$\begin{aligned}&a_1\phi_{M,e}\left(E,k_{M,ex}^{+,s}\right)e^{ik_{M,ex}^{+,s}L}+a_2\phi_{M,e}\left(E,-k_{M,ex}^{+,s}\right)e^{-ik_{M,ex}^{+,s}L}+a_3\phi_{M,e}\left(E,k_{M,ex}^{-,s}\right)e^{ik_{M,ex}^{-,s}L}+a_4\phi_{M,e}\left(E,-k_{M,ex}^{-,s}\right)e^{-ik_{M,ex}^{-,s}L}\\ &\quad+b_1\phi_{M,h}\left(E,k_{M,hx}^{+,s}\right)e^{ik_{M,hx}^{+,s}L}+b_2\phi_{M,h}\left(E,-k_{M,hx}^{+,s}\right)e^{-ik_{M,hx}^{+,s}L}+b_3\phi_{M,h}\left(E,k_{M,hx}^{-,s}\right)e^{ik_{M,hx}^{-,s}L}+b_4\phi_{M,h}\left(E,-k_{M,hx}^{-,s}\right)e^{-ik_{M,hx}^{-,s}L}\end{aligned}$$

$$= \left[t^{\eta,s}_{EC,\pm} u^{\eta,s}_R\left(E,\mp k^{\pm,s}_{R,ex}\right) e^{\mp i k^{\pm,s}_{R,ex} L} + t^{\eta,s}_{EC\mp} u^{\eta,s}_R u^{s}_R\left(E,\pm k^{\mp,s}_{R,ex}\right) e^{\pm i k^{\mp,s}_{R,ex} L}\right]\binom{1}{0}$$
$$+ \left[t^{\eta,s}_{\mathrm{CA}\pm} v^{\eta,s}_R\left(E,\pm k^{\pm,s}_{R,ex}\right) e^{\pm i k^{\pm}_{R,hx} L} + t^{\eta,s}_{\mathrm{CA},\mp} v^{\eta,s}_R\left(E,\mp k^{\mp,s}_{R,hx}\right) e^{\mp i k^{\mp,s}_{R,hx} L}\right]\binom{0}{1}. \tag{B2}$$

Solving Eqs. (B1) and (B2) for the scattering amplitudes $r^{\eta,s}_{N,\tau}$, $r^{\eta,s}_{\mathrm{A},\tau}$, $t^{\eta,s}_{\mathrm{EC},\tau}$, and $t^{\eta,s}_{\mathrm{CA},\tau}$, we find that the corresponding reflection and transmission probability coefficients equal

$$R^{\eta,s}_{N,\pm} = \left|r^{\eta,s}_{N,\pm}\right|^2, \quad R^{\eta,s}_{N,\mp} = \frac{V^{\eta,s}_{L\mp,ex}}{V^{\eta,s}_{L\pm,ex}}\left|r^{\eta,s}_{N\mp}\right|^2, \quad R^{\eta,s}_{A,\pm} = \frac{V^{\eta,s}_{L\pm,hx}}{V^{\eta,s}_{L\pm,ex}}\left|r^{\eta,s}_{A,\pm}\right|^2, \quad R^{\eta,s}_{A,\mp} = \frac{V^{\eta,s}_{L\mp,hx}}{V^{\eta,s}_{L\pm,ex}}\left|r^{\eta,s}_{A,\mp}\right|^2,$$
$$T^{\eta,s}_{EC,\pm} = \frac{V^{\eta,s}_{R\pm,ex}}{V^{\eta,s}_{L\pm,ex}}\left|t^{\eta,s}_{EC\pm}\right|^2, \quad T^{\eta,s}_{EC\mp} = \frac{V^{\eta,s}_{R\mp,ex}}{V^{\eta,s}_{L\pm,ex}}\left|t^{\eta,s}_{EC\mp}\right|^2, \quad T^{\eta,s}_{\mathrm{CA}\pm} = \frac{V^{\eta,s}_{R\pm,hx}}{V^{\eta,s}_{L\pm,ex}}\left|t^{\eta,s}_{\mathrm{CA}\pm}\right|^2, \quad T^{\eta,s}_{\mathrm{CA},\mp} = \frac{V^{\eta,s}_{R\mp,hx}}{V^{\eta,s}_{L\pm,ex}}\left|t^{\eta,s}_{\mathrm{CA},\mp}\right|^2, \tag{B3}$$

with

$$V^{\eta,s}_{L\pm,ex} = \left\langle u^{\eta,s}_L\left(E,\mp k^{\pm,s}_{L,ex}\right)\right| \frac{\partial H_e}{\hbar\partial k_x} \left|u^{\eta,s}_L\left(E,\mp k^{\pm,s}_{L,ex}\right)\right\rangle,$$
$$V^{\eta,s}_{L\pm,hx} = \left\langle v^{\eta,s}_L\left(E,\pm k^{\pm,s}_{L,hx}\right)\right| \frac{\partial H_h}{\hbar\partial k_x} \left|v^{\eta,s}_L\left(E,\pm k^{\pm,s}_{L,hx}\right)\right\rangle,$$
$$V^{\eta,s}_{R\pm,ex} = \left\langle u^{\eta,s}_R\left(E,\mp k^{\pm,s}_{R,ex}\right)\right| \frac{\partial H_e}{\hbar\partial k_x} \left|u^{\eta,s}_R\left(E,\mp k^{\pm,s}_{R,ex}\right)\right\rangle,$$
$$V^{\eta,s}_{R\pm,hx} = \left\langle v^{\eta,s}_R\left(E,\pm k^{\pm,s}_{R,ex}\right)\right| \frac{\partial H_h}{\hbar\partial k_x} \left|v^{\eta,s}_R\left(E,\pm k^{\pm,s}_{R,ex}\right)\right\rangle. \tag{B4}$$

These probability coefficients satisfy the identity $R^{\eta,s}_{N,\pm} + R^{\eta,s}_{N,\mp} + R^{\eta,s}_{A,\pm} + R^{\eta,s}_{A,\mp} + T^{\eta,s}_{EC,\pm} + T^{\eta,s}_{EC\mp} + T^{\eta,s}_{\mathrm{CA}\pm} + T^{\eta,s}_{\mathrm{CA},\mp} = 1$.

[1] J. M. Raimond, M. Brune, and S. Haroche, Rev. Mod. Phys. **73**, 565 (2001).

[2] C. H. Bennett and D. P. DiVincenzo, Nature (London) **404**, 247 (2000).

[3] R. Ursin, F. Tiefenbacher, T. Schmitt-Manderbach, H. Weier, T. Scheidl, M. Lindenthal, B. Blauensteiner, T. Jennewein, J. Perdigues, P. Trojek *et al.*, Nat. Phys. **3**, 481 (2007).

[4] J.-G. Ren, P. Xu, H.-L. Yong, L. Zhang, S.-K. Liao, J. Yin, W.-Y. Liu, W.-Q. Cai, M. Yang, L. Li *et al.*, Nature (London) **549**, 70 (2017).

[5] H. Wang, H. Hu, T.-H. Chung, J. Qin, X. Yang, J.-P. Li, R.-Z. Liu, H.-S. Zhong, Y.-M. He, X. Ding, Y.-H. Deng, Q. Dai, Y.-H. Huo, S. Hofling, C.-Y. Lu, and J.-W. Pan, Phys. Rev. Lett. **122**, 113602 (2019).

[6] A. Einstein, B. Podolsky, and N. Rosen, Phys. Rev. **47**, 777 (1935).

[7] M. D. Reid, P. D. Drummond, W. P. Bowen, E. G. Cavalcanti, P. K. Lam, H. A. Bachor, U. L. Andersen, and G. Leuchs, Rev. Mod. Phys. **81**, 1727 (2009).

[8] C. Bäuerle, D. C. Glattli, T. Meunier, F. Portier, P. Roche, P. Roulleau, S. Takada, and X. Waintal, Rep. Prog. Phys. **81**, 056503 (2018).

[9] C. W. J. Beenakker, in *Quantum Computers, Algorithms and Chaos, Proceedings of the International School of Physics "Enrico Fermi"* (IOS Press, Amsterdam, 2006), Vol. 162, p. 307.

[10] L. Hofstetter, S. Csonka, J. Nygård, and C. Schönenberger, Nature (London) **461**, 960 (2009).

[11] A. Das, Y. Ronen, M. Heiblum, D. Mahalu, A. V. Kretinin, and H. Shtrikman, Nat. Commun. **3**, 1165 (2012).

[12] A. Bergschneider, V. M. Klinkhamer, J. H. Becher, R. Klemt, L. Palm, G. Zürn, S. Jochim, and P. M. Preiss, Nat. Phys. **15**, 640 (2019).

[13] Y. Zhong, H.-S. Chang, K. Satzinger, M.-H. Chou, A. Bienfait, C. Conner, É. Dumur, J. Grebel, G. Peairs, R. Povey *et al.*, Nat. Phys. **15**, 741 (2019).

[14] D. Beckmann, H. B. Weber, and H. v. Löhneysen, Phys. Rev. Lett. **93**, 197003 (2004).

[15] Y. S. Ang, L. K. Ang, C. Zhang, and Z. Ma, Phys. Rev. B **93**, 041422 (2016).

[16] R. Beiranvand, H. Hamzehpour, and M. Alidoust, Phys. Rev. B **96**, 161403 (2017).

[17] P. L. Stroganov and Y. V. Fominov, Phys. Rev. B **96**, 174508 (2017).

[18] K. Bocian, W. Rudziński, and I. Weymann, Phys. Rev. B **97**, 195441 (2018).

[19] M. Veldhorst and A. Brinkman, Phys. Rev. Lett. **105**, 107002 (2010).

[20] J. Cayssol, Phys. Rev. Lett. **100**, 147001 (2008).

[21] F. Qi, J. Cao, and G. Jin, Phys. Rev. B **98**, 045422 (2018).

[22] R. W. Reinthaler, P. Recher, and E. M. Hankiewicz, Phys. Rev. Lett. **110**, 226802 (2013).

[23] J. J. He, J. Wu, T.-P. Choy, X.-J. Liu, Y. Tanaka, and K. T. Law, Nat. Commun. **5**, 3232 (2014).

[24] D. Breunig, P. Burset, and B. Trauzettel, Phys. Rev. Lett. **120**, 037701 (2018).

[25] J. Schindele, A. Baumgartner, and C. Schönenberger, Phys. Rev. Lett. **109**, 157002 (2012).

[26] R. Sánchez, P. Burset, and A. L. Yeyati, Phys. Rev. B **98**, 241414 (2018).
[27] R. Hussein, M. Governale, S. Kohler, W. Belzig, F. Giazotto, and A. Braggio, Phys. Rev. B **99**, 075429 (2019).
[28] L. G. Herrmann, F. Portier, P. Roche, A. L. Yeyati, T. Kontos, and C. Strunk, Phys. Rev. Lett. **104**, 026801 (2010).
[29] P. Burset, W. J. Herrera, and A. L. Yeyati, Phys. Rev. B **84**, 115448 (2011).
[30] B. Braunecker, P. Burset, and A. Levy Yeyati, Phys. Rev. Lett. **111**, 136806 (2013).
[31] A. Schroer, P. G. Silvestrov, and P. Recher, Phys. Rev. B **92**, 241404 (2015).
[32] S.-B. Zhang and B. Trauzettel, Phys. Rev. Lett. **122**, 257701 (2019).
[33] W. Chen, R. Shen, L. Sheng, B. G. Wang, and D. Y. Xing, Phys. Rev. Lett. **109**, 036802 (2012).
[34] J. Linder, M. Zareyan, and A. Sudbø, Phys. Rev. B **80**, 014513 (2009).
[35] G. Metalidis, M. Eschrig, R. Grein, and G. Schön, Phys. Rev. B **82**, 180503 (2010).
[36] J. Schindele, A. Baumgartner, R. Maurand, M. Weiss, and C. Schönenberger, Phys. Rev. B **89**, 045422 (2014).
[37] J. Nilsson, A. R. Akhmerov, and C. W. J. Beenakker, Phys. Rev. Lett. **101**, 120403 (2008).
[38] P. Samuelsson, E. V. Sukhorukov, and M. Büttiker, Phys. Rev. Lett. **91**, 157002 (2003).
[39] C. Beenakker, Phys. Rev. Lett. **97**, 067007 (2006).
[40] A. R. Akhmerov and C. W. J. Beenakker, Phys. Rev. Lett. **98**, 157003 (2007).
[41] T. Ludwig, Phys. Rev. B **75**, 195322 (2007).
[42] J. Linder and T. Yokoyama, Phys. Rev. B **89**, 020504 (2014).
[43] D. K. Efetov and K. B. Efetov, Phys. Rev. B **94**, 075403 (2016).
[44] A. Soori, M. R. Sahu, A. Das, and S. Mukerjee, Phys. Rev. B **98**, 075301 (2018).
[45] D. K. Mukherjee, J. Hutchinson, and A. Kundu, Phys. Rev. B **98**, 125424 (2018).
[46] A. F. Morpurgo and F. Guinea, Phys. Rev. Lett. **97**, 196804 (2006).
[47] S. V. Morozov, K. S. Novoselov, M. I. Katsnelson, F. Schedin, L. A. Ponomarenko, D. Jiang, and A. K. Geim, Phys. Rev. Lett. **97**, 016801 (2006).
[48] Y. Zhang, T.-T. Tang, C. Girit, Z. Hao, M. C. Martin, A. Zettl, M. F. Crommie, Y. R. Shen, and F. Wang, Nature (London) **459**, 820 (2009).
[49] C. Cardoso, D. Soriano, N. A. García-Martínez, and J. Fernández-Rossier, Phys. Rev. Lett. **121**, 067701 (2018).
[50] K. Zollner, M. Gmitra, and J. Fabian, New J. Phys. **20**, 073007 (2018).
[51] E. McCann and V. I. Fal'ko, Phys. Rev. Lett. **96**, 086805 (2006).
[52] A. H. Castro Neto, F. Guinea, N. M. R. Peres, K. S. Novoselov, and A. K. Geim, Rev. Mod. Phys. **81**, 109 (2009).
[53] E. McCann and M. Koshino, Rep. Prog. Phys. **76**, 056503 (2013).
[54] R. Kraft, I. V. Krainov, V. Gall, A. P. Dmitriev, R. Krupke, I. V. Gornyi, and R. Danneau, Phys. Rev. Lett. **121**, 257703 (2018).
[55] X. Li, Z. Zhang, and D. Xiao, Phys. Rev. B **81**, 195402 (2010).
[56] M. A. McGuire, H. Dixit, V. R. Cooper, and B. C. Sales, Chem. Mater. **27**, 612 (2015).
[57] S. Jiang, J. Shan, and K. F. Mak, Nat. Mater. **17**, 406 (2018).
[58] S. Jiang, L. Li, Z. Wang, K. F. Mak, and J. Shan, Nat. Nanotechnol. **13**, 549 (2018).
[59] M. Sui, G. Chen, L. Ma, W.-Y. Shan, D. Tian, K. Watanabe, T. Taniguchi, X. Jin, W. Yao, D. Xiao *et al.*, Nat. Phys. **11**, 1027 (2015).
[60] Z. Wang, Y.-H. Chiu, K. Honz, K. F. Mak, and J. Shan, Nano Lett. **18**, 137 (2018).
[61] J. O. Island, X. Cui, C. Lewandowski, J. Y. Khoo, E. M. Spanton, H. Zhou, D. Rhodes, J. C. Hone, T. Taniguchi, K. Watanabe *et al.*, Nature (London) **571**, 85 (2019).
[62] P. Rickhaus, G. Zheng, J. L. Lado, Y. Lee, A. Kurzmann, M. Eich, R. Pisoni, C. Tong, R. Garreis, C. Gold *et al.*, Nano Lett. **19**, 8821 (2019).
[63] L. Wang, I. Meric, P. Y. Huang, Q. Gao, Y. Gao, H. Tran, T. Taniguchi, K. Watanabe, L. M. Campos, D. A. Muller *et al.*, Science **342**, 614 (2013).
[64] M. Kim, J.-H. Choi, S.-H. Lee, K. Watanabe, T. Taniguchi, S.-H. Jhi, and H.-J. Lee, Nat. Phys. **12**, 1022 (2016).
[65] G. E. Blonder, M. Tinkham, and T. M. Klapwijk, Phys. Rev. B **25**, 4515 (1982).
[66] D. K. Efetov, L. Wang, C. Handschin, K. B. Efetov, J. Shuang, R. Cava, T. Taniguchi, K. Watanabe, J. Hone, C. R. Dean *et al.*, Nat. Phys. **12**, 328 (2015).
[67] C. Park, H. Yang, A. J. Mayne, G. Dujardin, S. Seo, Y. Kuk, J. Ihm, and G. Kim, Proc. Natl. Acad. Sci. USA **108**, 18622 (2011).
[68] B. Huang, G. Clark, E. Navarro-Moratalla, D. R. Klein, R. Cheng, K. L. Seyler, D. Zhong, E. Schmidgall, M. A. McGuire, D. H. Cobden *et al.*, Nature (London) **546**, 270 (2017).
[69] C. K. Chung and C. K. Law, Phys. Rev. A **78**, 034302 (2008).
[70] J. R. Schaibley, H. Yu, G. Clark, P. Rivera, J. S. Ross, K. L. Seyler, W. Yao, and X. Xu, Nat. Rev. Mater. **1**, 16055 (2016).